Journal of Electronic Imaging 9(4), 534–547 (October 2000).

Nonlinear resampling for edge preserving moiré suppression

Dimitri Van De Ville*
Koen Denecker
Ghent University
ELIS/MEDISIP
Sint Pietersnieuwstraat 41
B 9000 Ghent, Belgium
E-mail: dvdevill@elis.rug.ac.be

Wilfried Philips
Ghent University
TELIN
Sint Pietersnieuwstraat 41
B 9000 Ghent, Belgium

Ignace Lemahieu
Ghent University
ELIS/MEDISIP
Sint Pietersnieuwstraat 41
B 9000 Ghent, Belgium

Abstract. *Printing applications using classical halftoning need to resample the original image to a screen lattice. This resampling can cause undesirable moiré artifacts in the screened image. Some printing techniques, e.g., gravure printing, are highly susceptible to moiré, not only because of the low resolution screen lattices they employ but also because the degree of freedom in constructing halftone dots is limited by the physical constraints of the engraving mechanism. Current resampling methods compute new samples by simple interpolation techniques that cannot prevent sampling moiré very well. Therefore precautions against moiré have to be made in the prepress phase, which is not practical and sometimes not feasible. A novel technique is presented to adaptively resample an image on the screen lattice using a local estimate of the risk of aliasing. The purpose is to suppress moiré while maintaining the sharpness of the image. Experimental results demonstrate the feasibility of the proposed approach.*
[S1017-9909(00)01904-8]

1 Introduction

Moiré patterns arise from the interaction between two similar periodic patterns.[1–5] In some applications they can be used positively for the creation of special effects or for measuring small displacements. However, in the printing industry they are usually (very) undesirable because they are visually very disturbing.

The majority of today's printing techniques, including gravure printing, are binary processes: they produce bilevel images.[6] Halftoning techniques are required to create the illusion of continuous-tone images. These techniques rely on the human visual system that integrates small bilevel features to achieve an illusion of the original contone. There are essentially two classes of halftoning techniques. Most recently, frequency modulation is based on a stochastic distribution of small similar dots. Classical halftoning or amplitude modulation, on the other hand, places dots of varying sizes on a regular screen lattice. In particular, gravure printing is an example of classical halftoning with pure amplitude modulation. Each halftone dot corresponds with a little notch in the printing plate, engraved with a computer-driven diamond. The depth of such a notch determines the size of the corresponding halftone dot. The low resolution of the screen lattice renders gravure printing very susceptible to moiré formation: interaction of the periodic screen lattice with the contents of the original image may lead to sampling moiré caused by aliasing in the resampling process.[5] The regular dot shape due to pure amplitude modulation makes this moiré formation almost exclusively dependent on the resampling stage. In addition, high printing plate preparation costs (which make gravure printing only suitable for large volumes) make it essential to prevent moiré to avoid wasting printing plates.

*Author to whom correspondence should be addressed; research assistant of the FWO Flanders, Belgium.

Paper 99058 received Oct. 20, 1999; revised manuscript received June 15, 2000; accepted for publication June 29, 2000.
1017-9909/2000/$15.00

Current resampling techniques use simple interpolation techniques like bilinear interpolation, which cannot prevent sampling moiré when the original image contains high frequency components.[7–10] Of course, moiré patterns can be prevented by smoothing the original image since they are caused by aliasing. As is well known, smoothing corresponds to low-pass filtering in the frequency domain.[11] In the case of gravure printing, suppressing moiré requires a degree of smoothing that unacceptably blurs the image. One tactic to avoid moiré would be to selective blur the image in the high frequency regions. This selective blurring needs to be supervised at least in part by a human before resampling (i.e., in the prepress phase). Such an approach is time consuming, expensive and risky given the high cost of gravure printing plate production. Additionally, the required blurring depends on the gravure printing settings which are not always known in the prepress stage.

Several researchers have proposed halftoning techniques, that attempt to deal with the problem of sampling moiré. For instance, Roetling[12] proposes a halftoning method with moiré suppression. In this method, the average gray value of each halftone cell is kept identical to the average value of the corresponding part of the original image. In the case of gravure printing, where only the size but not the shape of a halftone dot can be changed, such an approach is similar to a slight smoothing, which neither suppresses moiré nor preserves edges very well. Defée[13] switches between a smoothing and a median filter to resample an image from an orthogonal lattice to another orthogonal lattice with halved resolutions. The switching scheme, based on heuristics, and the type of median filter are dependent on the specific source and target lattice, which constitutes a major drawback.

We present a novel technique to adaptively resample an image to an arbitrary target lattice. This technique locally combines two suitable linear resampling filters: the weight factors in this local linear combination are dependent on an estimate of the risk of aliasing. This estimate is based on general frequency analysis of the Nyquist areas of the involved lattices. The weight factor changes gradually to avoid abrupt transitions between one resampling filter and the other.

The paper is organized as follows. First some essential theory about lattices and resampling is introduced in Sec. 2. Section 3 then describes the new technique for the risk estimation and applies this technique to a novel resampling scheme. Experimental results using this new scheme are presented in Sec. 4. Because this paper is not printed using gravure printing, the resampled images are halftoned using a specially developed method that simulates gravure printing halftoning on common desktop printers. Figure 1 shows an example of this simulated gravure printing halftoning technique. The enlarged part clearly shows how gravure cells are constituted.

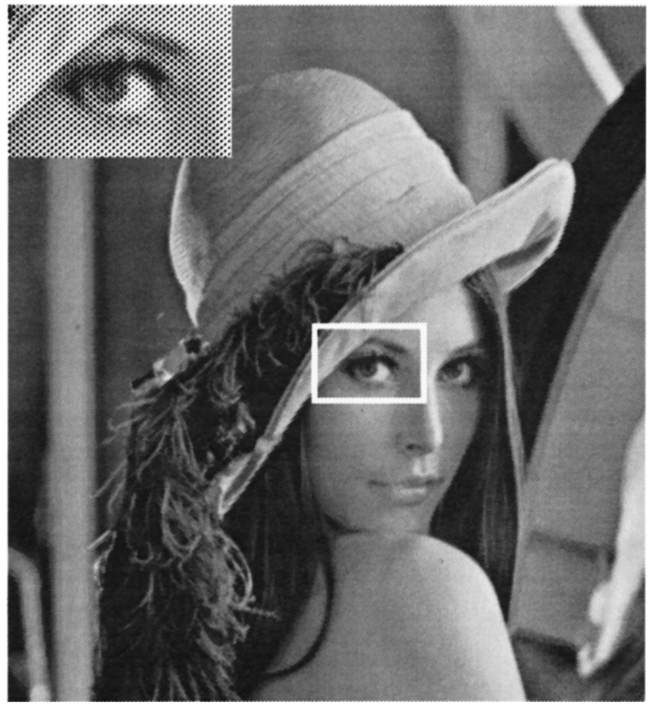

Fig. 1 Example of simulated gravure printing halftone.

2 Resampling

In the case of classical halftoning, the image is resampled from its source lattice to a target lattice, namely the screen lattice. During this process, moiré patterns can arise. To study this phenomenon, we now introduce lattice theory and sampling theory. We use lower case bold letters for (two-dimensional) vectors while uppercase bold letters refer to matrices.

2.1 Lattices and Sampling

A two-dimensional lattice can be characterized by two (linearly independent) vectors $\mathbf{r}_1$ and $\mathbf{r}_2$. Each lattice site is represented by the vector

$$\begin{aligned}\mathbf{r}_{m,n} &= m\mathbf{r}_1 + n\mathbf{r}_2, \quad \text{where } m,n \in \mathbb{Z}\\ &= (\mathbf{r}_1|\mathbf{r}_2)\begin{pmatrix} m \\ n \end{pmatrix}\\ &= \mathbf{Rm}, \quad \text{where } \mathbf{m} \in \mathbb{Z}^2. \end{aligned} \tag{1}$$

Thus the lattice is described by the matrix $\mathbf{R}$; it can also be described by the so-called Voronoi cell of the lattice $\mathbf{R}$, which is defined as the set of all points that are closer to the origin $(0\,0)^T$ than to any other site of the lattice. The Voronoi cell is often represented by its indicator function $\chi_{\mathbf{R}}(\mathbf{x})$

$$\chi_{\mathbf{R}}(\mathbf{x}) = \begin{cases} 1, & \mathbf{x} \in \text{Voronoi cell},\\ 1/k, & \mathbf{x} \text{ on edge Voronoi cell},\\ 0, & \mathbf{x} \notin \text{Voronoi cell}, \end{cases} \tag{2}$$

where k equals the number of lattice sites to which $\mathbf{x}$ is equidistant. Note that the Voronoi cell, when periodically copied onto all the lattice sites, covers the complete plane

$$\sum_{\mathbf{m}}^{\infty} \chi_{\mathbf{R}}(\mathbf{x} - \mathbf{Rm}) = 1, \quad \forall \mathbf{x} \in \mathbb{R}^2. \tag{3}$$

It is said that the Voronoi cell tiles the plane. The reciprocal lattice is defined as the lattice with matrix $\mathbf{F} = (\mathbf{R}^{-1})^T$; its importance will become clear soon.

Consider an image $i(\mathbf{x})=i(x_1,x_2)$ in the domain $\mathbb{R}^2$. The spectrum $I(\mathbf{f})$ of $i(\mathbf{x})$ is its two-dimensional Fourier transform

$$I(\mathbf{f})=\mathcal{F}\{i(\mathbf{x})\}(\mathbf{f})=\int_{\infty} i(\mathbf{x})e^{-j2\pi\mathbf{f}\cdot\mathbf{x}}d\mathbf{x}. \tag{4}$$

Sampling the image $i(\mathbf{x})$ on a lattice $\mathbf{R}$ is equivalent to ''taking out'' the values of $i(\mathbf{x})$ for $\mathbf{x}$ on the sampling lattice. However, it is convenient to introduce $i_S(\mathbf{x})$, a function which is still defined for all $\mathbf{x}$ and not only for $\mathbf{x}\in\mathbf{R}$. The so-called ''sampled image'' $i_S(\mathbf{x})$ is then nonzero only on the lattice sites. This ''point source'' representation is mathematically modeled using Dirac impulses $\delta(\mathbf{x})$

$$i_S(\mathbf{x})=i(\mathbf{x})\sum_{\mathbf{m}}^{\infty}\delta(\mathbf{x}-\mathbf{Rm}). \tag{5}$$

Note that although the point sources $\delta(\mathbf{x}-\mathbf{Rm})$ are infinite, the integrated value over the area G associated with the Voronoi cell around the lattice site at $\mathbf{Rm}$ is still the original image value $i(\mathbf{Rm})$

$$\int_G i_S(\mathbf{y})d\mathbf{y}=i(\mathbf{Rm}). \tag{6}$$

The advantage of using the sampled image $i_S(\mathbf{x})$ is that it allows us to relate the spectrum of the sampled image $I_S(\mathbf{f})$ to the original spectrum $I(\mathbf{f})$. In particular, due to the sampling, the spectrum $I(\mathbf{f})$ is replicated in the frequency domain according to[6,14]

$$I_S(\mathbf{f})=\frac{1}{|\det(\mathbf{R})|}\sum_{\mathbf{n}}^{\infty} I(\mathbf{f}-\mathbf{Fn}), \tag{7}$$

where $\mathbf{F}$ is the reciprocal matrix of $\mathbf{R}$. If the ''replicas'' $I(\mathbf{f}-\mathbf{Fm})$ in Eq. (7) overlap, aliasing occurs and high frequency patterns are mapped onto low frequency regions. Overlap does not occur when $I(\mathbf{f})$ is nonzero only for the Voronoi cell of $\mathbf{F}$. The Voronoi cell of the reciprocal sampling lattice is also called the Nyquist area.

2.2 *Gravure Printing Lattices*

The halftoning process involved in gravure printing can be conceptually split into two stages. First the image is resampled from the original lattice to the screen lattice. Second each sample is used to engrave the corresponding notch in the printing plate. Figure 2 shows the result after each of these two stages.

The lattice of the original digital image is orthogonal: its matrix $\mathbf{R}$ and reciprocal matrix $\mathbf{F}$ are

$$\mathbf{R}=\begin{pmatrix} r & 0\\ 0 & r\end{pmatrix},\quad \mathbf{F}=\begin{pmatrix} 1/r & 0\\ 0 & 1/r\end{pmatrix}, \tag{8}$$

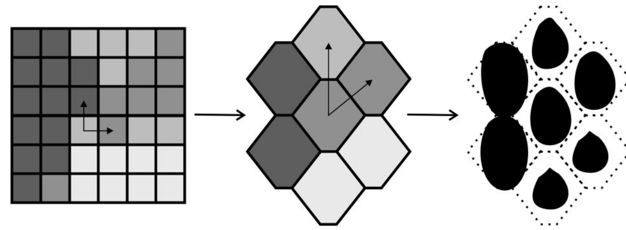

Fig. 2 Gravure printing halftoning split into two stages.

where $1/r$ is the horizontal and vertical resolution of the image. On the other hand, the screen lattice is not rectangular but semiregular hexagonal, i.e., its lattice matrix $\mathbf{V}$ and reciprocal matrix $\mathbf{W}$ are

$$\mathbf{V}=\begin{pmatrix} 0 & b\\ a & a/2\end{pmatrix},\quad \mathbf{W}=\begin{pmatrix} -1/(2b) & 1/b\\ 1/a & 0\end{pmatrix}. \tag{9}$$

For the type of gravure printing we consider, the values of a and b are 0.2 and 0.12 mm. Consequently the numerical values of the reciprocal matrices of the original lattice and the screen lattice are

$$\mathbf{F}=\begin{pmatrix} 300 & 0\\ 0 & 300\end{pmatrix}\ \text{dpi}, \tag{10}$$

$$\mathbf{W}=\begin{pmatrix} -105.8 & 211.6\\ 127 & 0\end{pmatrix}\ \text{dpi}. \tag{11}$$

Figure 3 shows the Voronoi cells of these lattices and the corresponding reciprocal lattices, the corresponding indicator functions are:

- $\chi_{\mathbf{R}}(\mathbf{x})$: spatial Voronoi cell of the source lattice,
- $\chi_{\mathbf{F}}(\mathbf{f})$: reciprocal Voronoi cell of the source lattice,
- $\chi_{\mathbf{V}}(\mathbf{x})$: spatial Voronoi cell of the target lattice,
- $\chi_{\mathbf{W}}(\mathbf{f})$: reciprocal Voronoi cell of the target lattice.

2.3 *Linear Resampling*

Resampling computes new samples on a target lattice from the original samples on the source lattice. Conceptually, it can be viewed as a two-step process. First a continuous image is reconstructed by interpolating the samples of the original image. In the particular case of linear resampling,

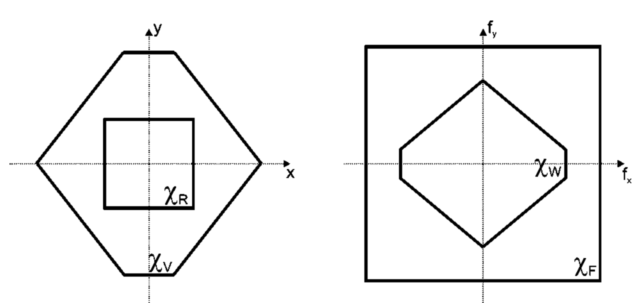

Fig. 3 The Voronoi cells in the spatial and the spectral domain in the case of gravure printing halftoning.

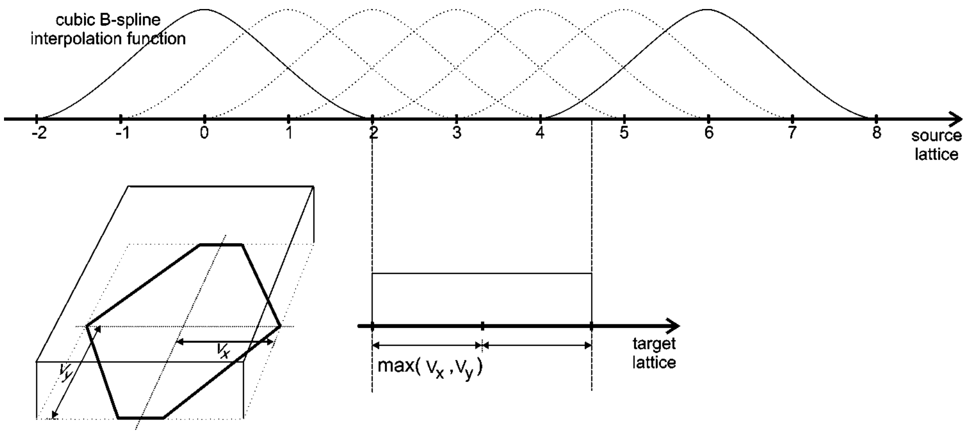

Fig. 4 A 7×7 support is obtained when applying the principle of ''surface projection'' to the cubic *B*-spline interpolation function for our gravure printing settings.

the continuous image is calculated by convolving the sampled image $i_S(\mathbf{x})$ with the interpolation function $g(\mathbf{x})$

$$(i_S\otimes g)(\mathbf{x})=\sum_{\mathbf{m}}^{\infty} i_S(\mathbf{Rm})g(\mathbf{x}-\mathbf{Rm}). \tag{12}$$

Next the reconstructed image is sampled on the sites of the new lattice $\mathbf{V}$, which results in a resampled image, nonzero only at the target lattice sites

$$h_S(\mathbf{x})=(i_S\otimes g)(\mathbf{x})\sum_{\mathbf{k}}^{\infty} \delta(\mathbf{x}-\mathbf{Vk}). \tag{13}$$

Two frequently used and well known interpolation methods are nearest neighbor interpolation (pixel skipping and sample-and-hold) and bilinear interpolation.[7,8] The first one simply assigns the value of the nearest original sample to a target sample. This corresponds to the special choice $g(\mathbf{x})=\chi_{\mathbf{R}}(\mathbf{x})$ in Eq. (12). The second interpolation technique uses the distances to the neighboring original lattice sites as linear weighting factors of the original samples. For an orthogonal lattice this corresponds to the interpolation function $g(\mathbf{x})=(\chi_{\mathbf{R}}\otimes\chi_{\mathbf{R}})(\mathbf{x})$ in Eq. (12). The results in Sec. 4 show these resampling techniques are not adequate: clearly visible moiré patterns arise in high frequency regions of an image.

Fortunately interpolation can prevent moiré due to resampling to some degree when the interpolation function has a low-pass spectrum. The reconstruction of Eq. (12) can be viewed as a filter operation by the interpolation function: according to the convolution theorem the Fourier transform $\mathcal{F}\{i_S\otimes g\}(\mathbf{f})$ of the left-hand side of Eq. (12) equals the Fourier transform of the sampled image $I_S(\mathbf{f})$ times $G(\mathbf{f})$. If the spectrum $G(\mathbf{f})$ has sufficient low-pass characteristics, high frequency patterns are suppressed in the reconstructed image and moiré formation is prevented. ''Surface projection'' is a class of interpolation functions that incorporates low-pass filtering fitted to the target lattice. Consider a particular interpolation function $\hat{g}(\mathbf{x})$ which is used to reconstruct a continuous image from the sampled image as is done in Eq. (12). Instead of sampling this reconstructed image, an additional conceptual step is incorporated: the reconstruction is averaged over the target lattice's Voronoi cell around the target sample in order to obtain extra low-pass characteristics adapted to the target lattice. Mathematically the values of the target samples can then be written as

$$h_S(\mathbf{Vk})=c\int_{\infty}(i_S\otimes\hat{g})(\mathbf{x})\chi_{\mathbf{V}}(\mathbf{Vk}-\mathbf{x})d\mathbf{x}, \tag{14}$$

where $c=1/|\det(\mathbf{V})|$ is a normalization term, which equals the inverse of the surface area $|\det(\mathbf{V})|$ of the Voronoi cell. Equation (14) can be written in the form of Eq. (13) by defining $g(\mathbf{x})=(\hat{g}\otimes\chi_{\mathbf{V}})(\mathbf{x})$.

The best results for moiré suppression for our choice of screen lattice are obtained by using the cubic *B*-spline interpolation function[8,9,15] together with the principle of ''surface projection.'' Figure 4 shows in the upper part how the cubic *B*-spline interpolation function is placed upon every sample of the source lattice. The extra averaging using the target lattice's Voronoi cell (lower part of Fig. 4) further extends the support. The values of v_x and v_y can be calculated using geometry

$$v_x=\frac{4b^2+a^2}{8b},\quad v_y=\frac{a}{2}. \tag{15}$$

In total 7×7 original samples contribute to a target sample for our particular lattice settings. The results in Sec. 4 will show moiré is well suppressed but the global smoothing unacceptably degrades image quality.

3 Nonlinear Resampling

Choosing the optimal linear filter involves trading off antialiasing against blurring. Currently, bilinear interpolation is the most widely used technique in gravure printing. We present a novel resampling scheme that performs selective smoothing automatically. Our resampling scheme estimates the risk of aliasing and uses this estimate to adapt the de-

Table 1 Several window functions w_m.

	Definition
Square	$w_m=1$
Bartlett	$w_m=1-\left\lvert\frac{m-N/2}{N/2}\right\rvert$
Welch	$w_m=1-\left(\frac{m-N/2}{N/2}\right)^2$
Hann	$w_m=\frac{1-\cos(2\pi m/N)}{2}$

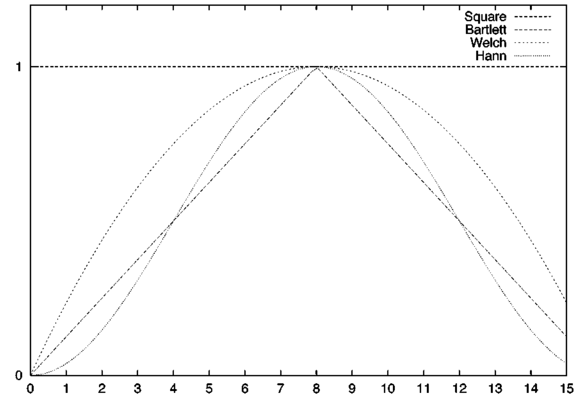

(a)

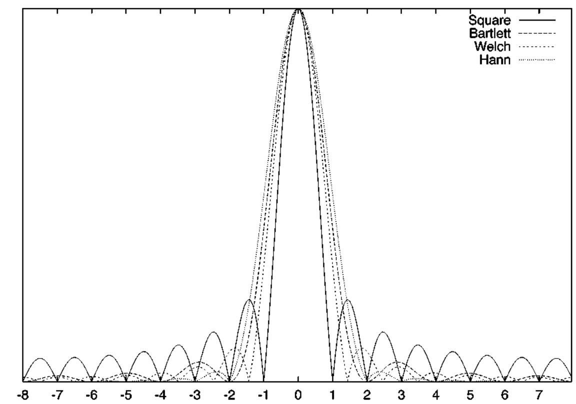

(b)

Fig. 5 (a) Different window functions w_m and (b) their frequency response $|W(f)|$.

gree of smoothing. We will first explain how the risk is estimated in a generic way and then how it can be applied to obtain better resampling quality.

3.1 *Estimation of the Risk of Aliasing*

This section introduces our technique to estimate the risk that aliasing will occur in the vicinity of a given pixel when the original image is resampled on the target lattice. This risk is a numerical value in the interval $[0,1]$ that should be high in regions where moiré patterns appear and low elsewhere. The technique is based on frequency analysis. Since we are in particular interested in local frequency characteristics, we compute the local spectrum using a windowed Fourier transform (short-time Fourier transform in the case of time signals). In this technique, a window of $N\times N$ pixels slides over the image and the discrete Fourier transform (DFT) is computed on this window. Section 3.1.1 will first derive the risk of frequencies that can occur in such a window. Next, Sec. 3.1.2 will apply these results to the whole image.

3.1.1 *Derivation of the risk matrix*

A digital image is composed of different frequency components, each of which contributes differently to the risk of aliasing. We first compute the risk for a single frequency component and we will deal with the general case afterwards.

Consider an image $i(\mathbf{x})$ consisting of a single sinusoidal component of frequency $\mathbf{f}_0$; thus its spectrum equals $I(\mathbf{f})=\delta(\mathbf{f}-\mathbf{f}_0)$. When this image is windowed and sampled on the lattice sites $\mathbf{r}_{m,n}=\mathbf{Rm}$ of an $N\times N$ window (the window indices are $(m,n)\in A=\{0,1,\ldots,N-1\}\times\{0,1,\ldots,N-1\}$), one can write

$$i_S(\mathbf{x})=i(\mathbf{x})\sum_{\mathbf{m}\in A}\delta(\mathbf{x}-\mathbf{Rm})w_{\mathbf{m}}=i(\mathbf{x})w(\mathbf{x}), \tag{16}$$

where the function $w(\mathbf{x})$ contains Dirac impulses with weights $w_{\mathbf{m}}$ and is thus the sampling and window function. The window functions $w_{\mathbf{m}}$ we consider are separable and real valued: $w_{\mathbf{m}}=w_{m_1}w_{m_2}$. Table 1 shows the window functions we examine later on.[16]

According to the convolution theorem, the spectrum of Eq. (16) equals

$$I_S(\mathbf{f})=(I\otimes W)(\mathbf{f}) \tag{17}$$

with

$$\begin{aligned}W(\mathbf{f})&=\int_\infty\sum_{\mathbf{m}\in A}\delta(\mathbf{x}-\mathbf{Rm})e^{-j2\pi\mathbf{f}\cdot\mathbf{x}}w_{\mathbf{m}}d\mathbf{x}\\&=\sum_{\mathbf{m}\in A}e^{-j2\pi\mathbf{f}\cdot\mathbf{Rm}}w_{\mathbf{m}}\\&=\sum_{m_1=0}^{N-1}e^{-j2\pi m_1\mathbf{f}\cdot\mathbf{r}_1}w_{m_1}\sum_{m_2=0}^{N-1}e^{-j2\pi m_2\mathbf{f}\cdot\mathbf{r}_2}w_{m_2}.\end{aligned} \tag{18}$$

Note that when we replace $\mathbf{f}$ by $\mathbf{f}-\mathbf{Fk}$, we obtain the same result due to $(\mathbf{f}-\mathbf{Fk})\cdot\mathbf{r}_1=\mathbf{f}\cdot\mathbf{r}_1-\mathbf{k}\cdot(1\ 0)^T$ and $(\mathbf{f}-\mathbf{Fk})\cdot\mathbf{r}_2=\mathbf{f}\cdot\mathbf{r}_2-\mathbf{k}\cdot(0\ 1)^T$. As a consequence, it is clear that $W(\mathbf{f})$ is periodic on the reciprocal lattice $\mathbf{F}$ of the original sampling lattice $\mathbf{R}$

$$W(\mathbf{f})=W(\mathbf{f}-\mathbf{Fk}),\quad\forall\mathbf{k}\in\mathbb{Z}^2. \tag{19}$$

Figure 5 shows several window functions and their frequency response according to Eq. (18). The horizontal axis in Fig. 5(b) corresponds to the frequency bin number. All the window functions have oscillatory lobes. This results in ‘‘frequency leakage’’ from one frequency bin to another: indeed, because of the convolution by $W(\mathbf{f})$ in Eq. (17) different window functions lead to different frequency responses, and thus to different leakage characteristics. Sev-

Table 2 Risk matrix Υ for $N=16$ and Hann window.

dpi	0	18.75	...					150
0	0.00	0.00	0.00	0.00	0.00	0.14	0.69	1.00	1.00
18.75	0.00	0.00	0.00	0.00	0.03	0.27	0.78	1.00	1.00
	0.00	0.00	0.00	0.05	0.30	0.71	0.96	1.00	1.00
⋮	0.00	0.00	0.08	0.38	0.79	0.97	1.00	1.00	1.00
	0.02	0.12	0.46	0.84	0.99	1.00	1.00	1.00	1.00
	0.29	0.56	0.89	0.99	1.00	1.00	1.00	1.00	1.00
	0.85	0.94	1.00	1.00	1.00	1.00	1.00	1.00	1.00
	1.00	1.00	1.00	1.00	1.00	1.00	1.00	1.00	1.00
150	1.00	1.00	1.00	1.00	1.00	1.00	1.00	1.00	1.00

eral figures of merit exist to numerically evaluate different windows.[16] We will use a criterion that is better suited for our application in Sec. 3.1.2.

We define the risk of aliasing for a frequency component $\mathbf{f}_0$ when it is resampled to the target lattice $\mathbf{V}$ as the fraction of the energy of $I_S(\mathbf{f})$ outside the Nyquist area of the target lattice $\mathbf{V}$ (or in other words outside the Voronoi cell of the reciprocal target lattice). Since $W(\mathbf{f})$ is periodic, computing this proportion over the whole plane is the same as over one period. Consequently, this risk can be written as

$$\upsilon(\mathbf{f}_0)=\frac{\int_{\chi_\mathbf{F}}|W^2(\mathbf{f}-\mathbf{f}_0)|(1-\chi_\mathbf{W}(\mathbf{f}))\,d\mathbf{f}}{\int_{\chi_\mathbf{F}}|W^2(\mathbf{f}-\mathbf{f}_0)|\,d\mathbf{f}}. \tag{20}$$

In general, the original image contains more than one frequency component and these components can be computed using a DFT.[11,16] The DFT coefficients estimate the spectrum at the frequencies

$$\mathbf{f}_{k,l}=\frac{k\mathbf{f}_1+l\mathbf{f}_2}{N}, \tag{21}$$

where the reciprocal lattice is $\mathbf{F}=(\mathbf{f}_1|\mathbf{f}_2)$. The corresponding DFT coefficients $I_{k,l}$ are

$$\begin{aligned}I_{k,l}&=I_S(\mathbf{f}_{k,l})\\&=\int_\infty I(\mathbf{f})W(\mathbf{f}_{k,l}-\mathbf{f})\,d\mathbf{f}\\&=\sum_{m=0}^{N-1}\sum_{n=0}^{N-1} i(\mathbf{r}_{m,n})e^{-j2\pi mk/N}w_m e^{-j2\pi nl/N}w_n.\end{aligned} \tag{22}$$

The risks $\upsilon(\mathbf{f}_{k,l})=\upsilon_{k,l}$ associated with each of the corresponding components can be computed using Eq. (20) and then arranged in a matrix Υ. In gravure printing, the symmetry of $\chi_\mathbf{F}(\mathbf{f})$ and $\chi_\mathbf{W}(\mathbf{f})$ (see Fig. 3) around both axes of the frequency domain reduces the calculation of the risks to one quadrant. The matrix

$$\Upsilon=(\upsilon_{l,k}),\quad k,l=0,\ldots,N/2 \tag{23}$$

is called the risk matrix. Notice that this matrix is device dependent but does not depend on the image. All we need to know to calculate and store the risk matrix are the lattice arrangements, the value of N, and the window function. Table 2 shows Υ for the case $N=16$ and a Hann window. The borders show the horizontal and vertical frequencies to which the risk coefficients correspond.

3.1.2 *Using the risk matrix to estimate the risk of aliasing*

Now consider an $N\times N$ window which slides over the image pixel by pixel. The total risk of aliasing associated with any given pixel is computed as follows:

1. Compute the windowed DFT.
2. Calculate the periodogram by putting every DFT coefficient $I_{k,l}$ to the square.
3. The risk of aliasing for the considered pixel is then defined as the proportion of the weighted energy coefficients (by the risk matrix Υ) to the total energy

$$\eta=\frac{\Sigma_{(k,l)\in A}I_{k,l}^2\upsilon_{k\oslash N,l\oslash N}}{\Sigma_{(k,l)\in A}I_{k,l}^2}, \tag{24}$$

where the $\oslash$ operator unfolds the risk matrix again to the four quadrants as follows:

$$k\oslash N=\begin{cases}k, & 0\leqslant k\leqslant N/2\\ N-k, & N/2<k\leqslant N-1.\end{cases} \tag{25}$$

In Eq. (24) A stands for the set of indices $\{0,1,\ldots,N-1\}\times\{0,1,\ldots,N-1\}$ of the DFT coefficients.

It is important to subtract the dc component from the pixels in the input window. Since pixel values are given in a positive interval, dc components—representing the average window value—are relatively large compared to other frequency components and disrupt the proportion of Eq. (24). Note that this must be done in advance of step 1, since the window function (except the implicit square window) spreads a large dc component over several neighboring frequency bins.

The risks of the different pixels of the image can be arranged in a so-called ''risk image'' which has the same dimensions as the original image. We will display such risk

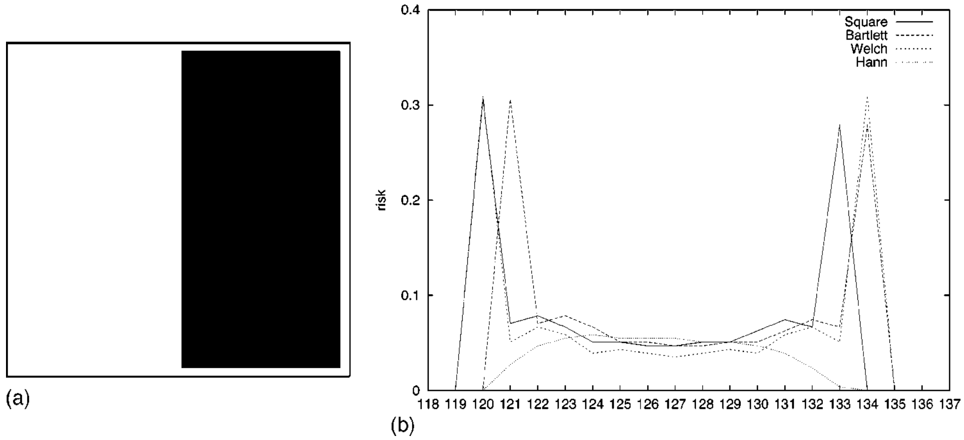

Fig. 6 (a) ''Edge'' test image and (b) the risk values in the neighborhood of the edge.

images as grayscale images with the convention that black and white gray values correspond to unity and zero risk, respectively.

Several parameters need to be fixed before the risk values of an image can be calculated. First of all, the value of N determines the window size. A larger value increases computation time (since the window for which the DFT is computed slides pixel by pixel) and decreases the spatial accuracy. On the other hand, it improves frequency resolution. In our experiments, we fix the window size at $N=16$ based on experiments with $N=8,16,32$. Further research could give more information about the influence of N. For example, the tradeoff between window size and computation time could be relaxed by a larger step of the window in the spatial domain.

A second even more important issue is the selection of the window function. The window functions are evaluated based on two criteria: ''edge response'' and ''zoneplate response.''

The ''edge response'' criterion expresses that the risk should be high in regions of high frequency patterns, but not on edges since we do not want to smooth them like high frequency patterns. Figure 6(a) shows a test image (256×256) with a sharp vertical edge at x coordinate 128. Figure 6(b) shows a horizontal crosscut of the risk image around the edge position. It appears that most window functions, including the square window, have a maximum risk of about $\eta_{\max}=0.3$ in the neighborhood of edges. These high risk values are found at a distance of $N/2$ pixels from the actual edge. In that situation, an edge inside the window does not appear as an edge anymore, but as a single impulse at the border of the window. The Hann window is our best choice because it has the weakest response on edges, especially at the border. The maximum value $\eta_{\max}$ stays below 0.06.

The ''zoneplate response'' criterion examines the risk images for the ''zoneplate'' and compares them to an ''ideal'' response. Figure 7(a) shows the zoneplate, which is a synthetic test image with increasing frequencies in both directions. The top left corner corresponds to the zero spatial frequency, the right and bottom border correspond to the frequencies at the border of the Nyquist area. Since the elements of the risk matrix in Eq. (20) are computed using the target lattice's Nyquist area as a criterion, we should ideally expect the risk to be 1 outside the Nyquist area, and 0 inside the Nyquist area, as it is shown in Fig. 7(b). Figure 8 shows the risk images using the different window functions. The risk image using the square window clearly shows blocking artifacts. The Bartlett and Welch windows perform slightly better. The Hann window provides a smooth transition. Figure 9 shows the absolute difference between the risk images and the ideal response of Fig. 7(b). The Nyquist area of the target lattice is best approached for the Hann window. Also, a numerical measure such as the

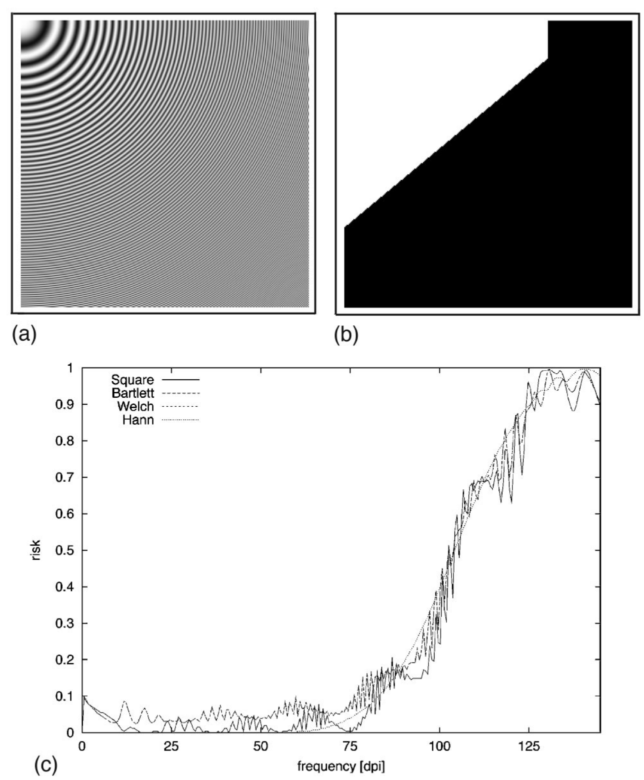

Fig. 7 (a) ''Zoneplate'' test image, (b) the ''ideal'' zoneplate response, and (c) the risk values in the horizontal crosscut on top of the risk images.

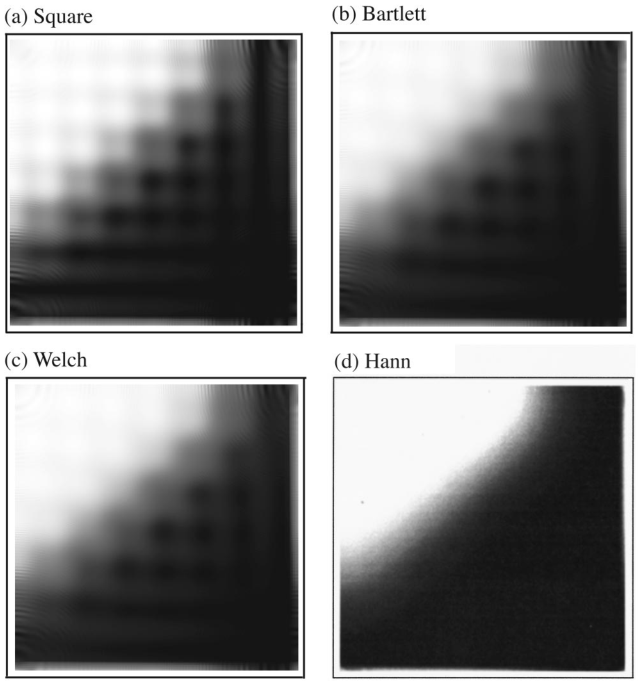

Fig. 8 Estimation of the risk of aliasing for ''zoneplate'' using different window functions (a)–(d).

mean-squared error between the risk images and the ideal response gives the best results for the Hann window. Figure 7(c) considers a horizontal crosscut at the top of the different risk images. These results clearly indicate the square window has large fluctuations where they are not expected.

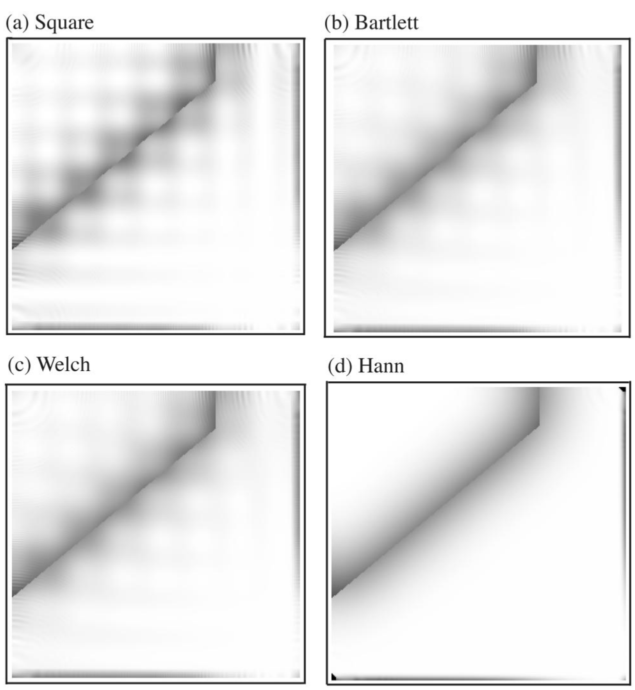

Fig. 9 Absolute difference between the risk images of Fig. 8 and the ''ideal'' response of Fig. 7 (b).

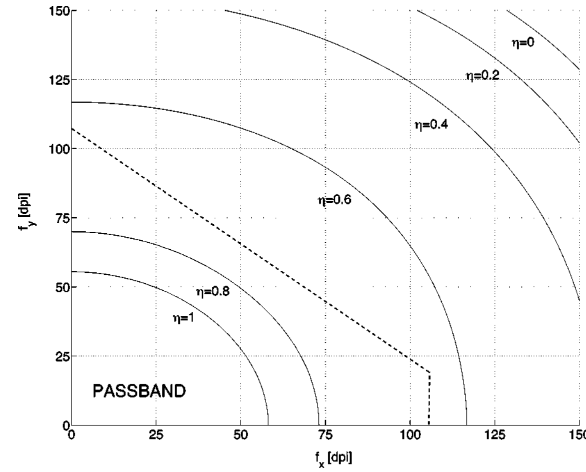

Fig. 10 Half amplitude (-6 dB) contour in the frequency plane of the combined interpolation filter for various values of the risk of aliasing η.

The Bartlett window and the Welch window do not improve this result much, while the Hann window again shows satisfactory results.

Both the ''edge response'' and the ''zoneplate response'' criterion prefer the Hann window. A low response on and near edges will instruct the resampling scheme of Sec. 3.2 not to use a moiré suppressing (smoothing) resampling filter, and will thus preserve edges. A good resemblance of the zoneplate risk image to the ideal response ensures the risk behaves as our initial criterion (the Nyquist area of the target lattice) imposed.

The current risk estimation scheme can not be applied as such to ''natural'' images. The proportion of Eq. (24) is not robust when its denominator is low. If that occurs, the estimate of the risk becomes inaccurate and dependent on noise. In practice, it is sufficient to put the risk to zero when the denominator is below the threshold value of $0.1N^2$. This value was determined experimentally and its value does not have a strong influence. The results in Sec. 4 will show how this adjustment modifies the risk images.

Our final scheme can now be summarized. An $N \times N$ windows slides pixel by pixel across the original image. For each window, the windowed DFT coefficients are computed after the dc coefficient is removed from the input data. Next, the proportion between the weighted periodogram, using the risk matrix, and the total periodogram energy is used as an estimate of the risk of aliasing for the central pixel of the window. If the denominator of the risk is below a certain threshold value, the risk is zeroed.

3.2 *A Novel Resampling Scheme*

Our goal is to use the estimate of the risk of aliasing to obtain a better resampled image. For that purpose we vary the amount of low-pass filtering according to the estimate of the risk. Thus smoothing can be restricted to the areas where it is needed. Specifically the new resampling scheme computes a weighted filter as a linear combination of the bilinear interpolation function [which is good as the edge-preserving (EP) filter and should be used in areas not susceptible to moiré] and the surface projected cubic B-spline filter [which suppresses moiré (MS) but also blurs edges]

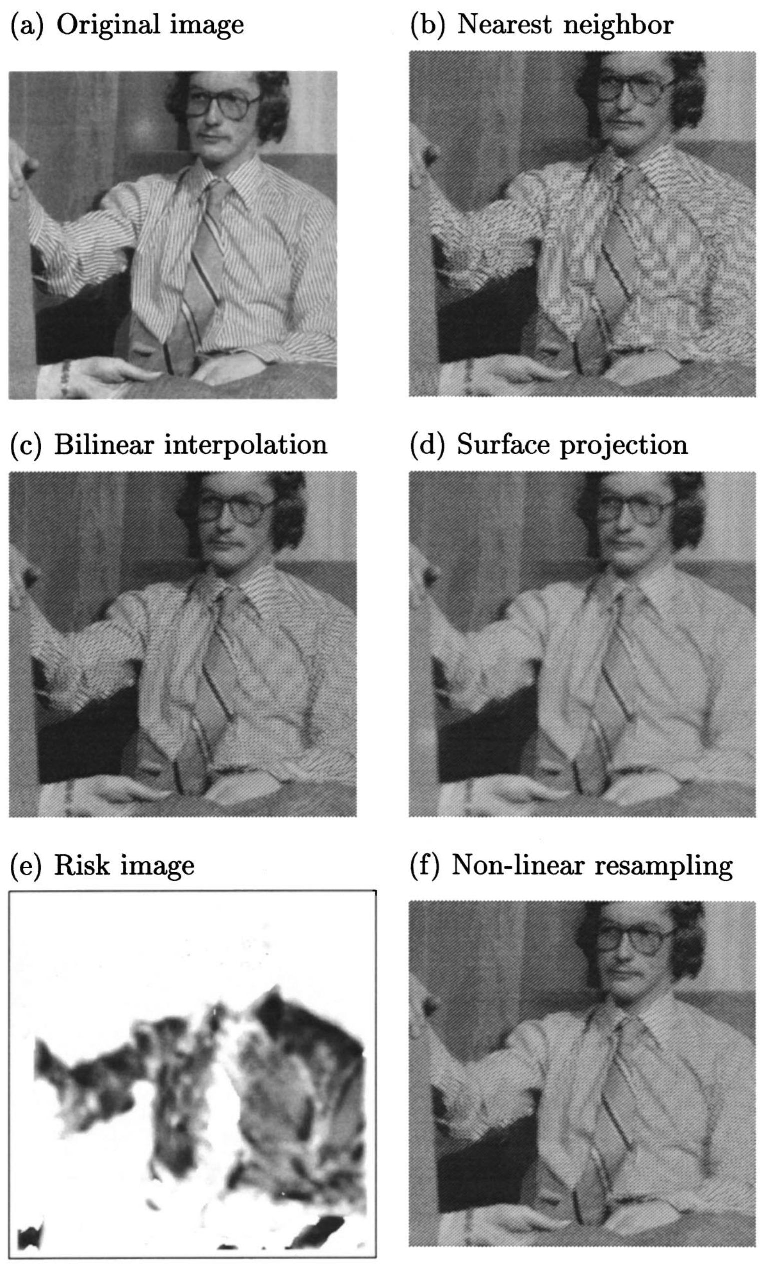

Fig. 11 (a) Original image ''shirt'' with (b)–(d) linear resampled versions, (e) risk image, and (f) result after nonlinear resampling.

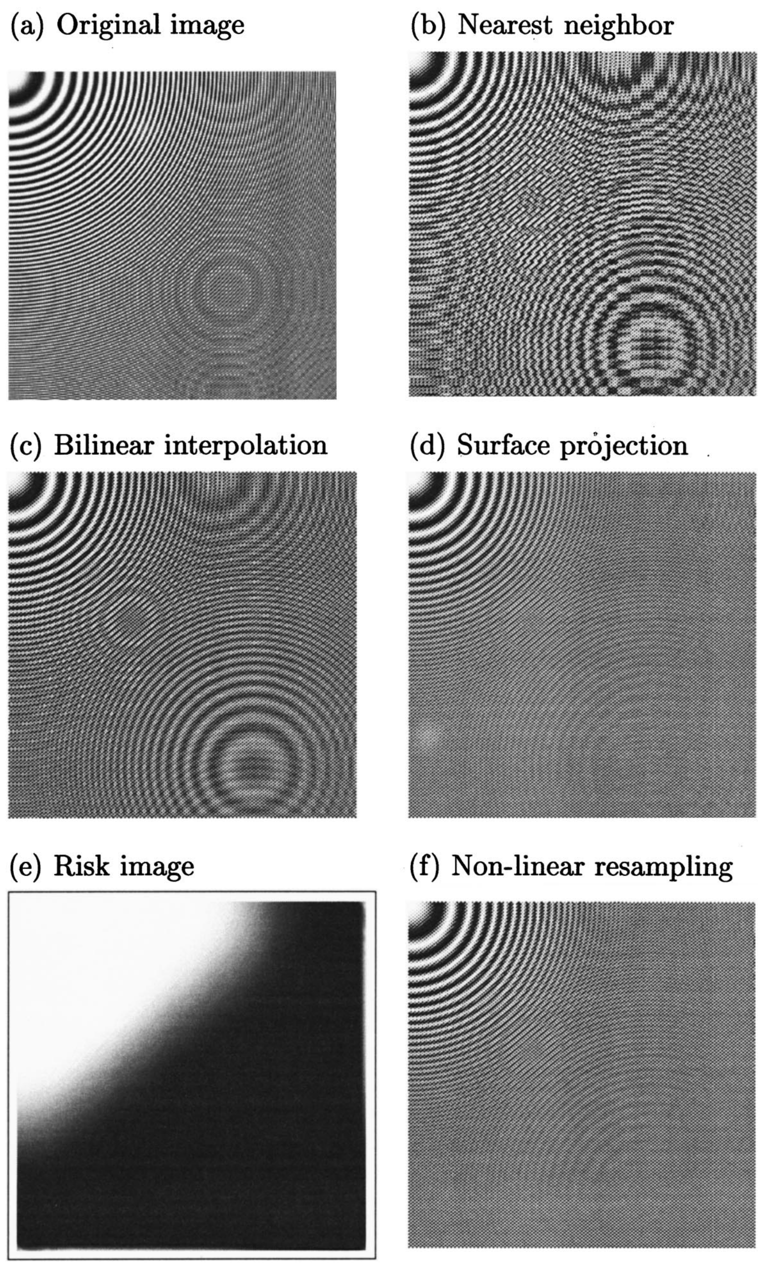

Fig. 12 (a) Original image ''zoneplate'' with (b)–(d) linear resampled versions, (e) risk image, and (f) result after nonlinear resampling.

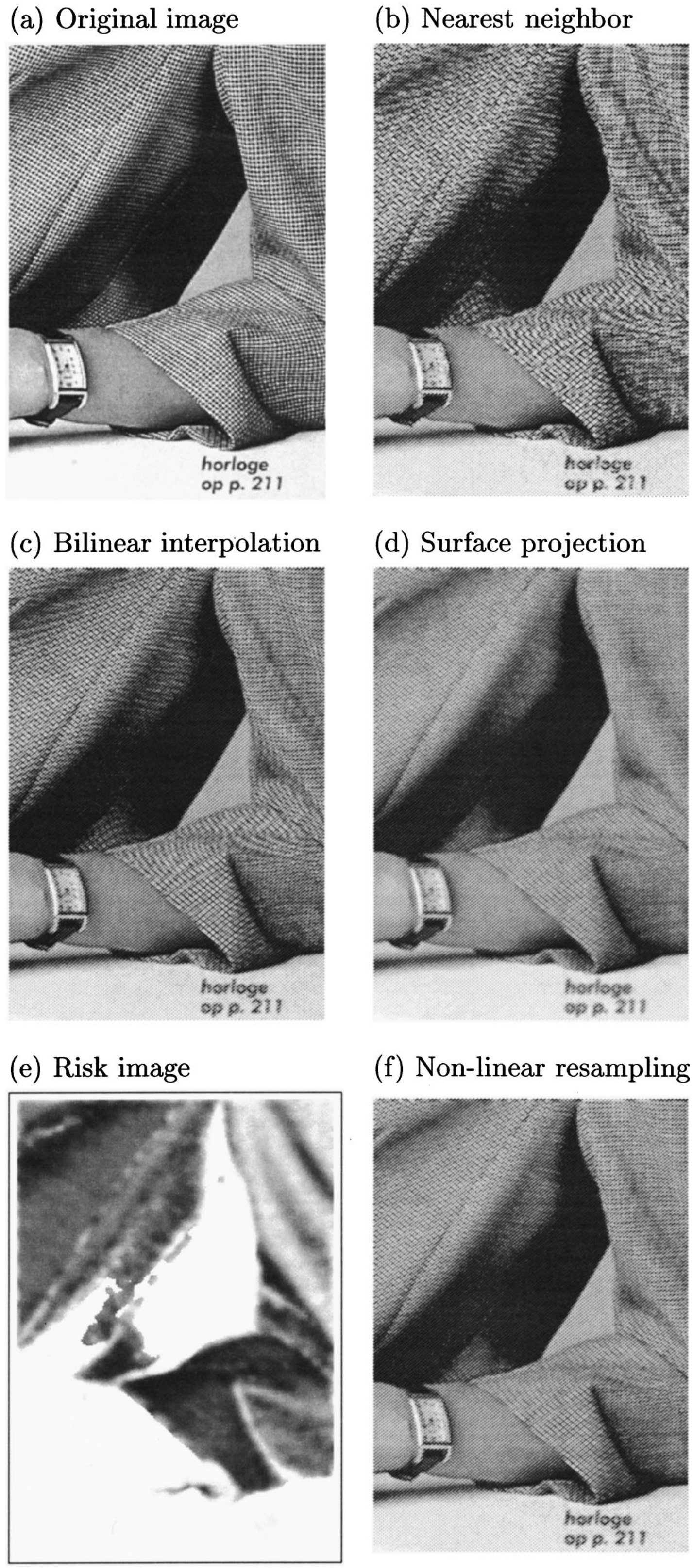

Fig. 13 (a) Original image ''horloge'' with (b)–(d) linear resampled versions, (e) risk image, and (f) result after nonlinear resampling.

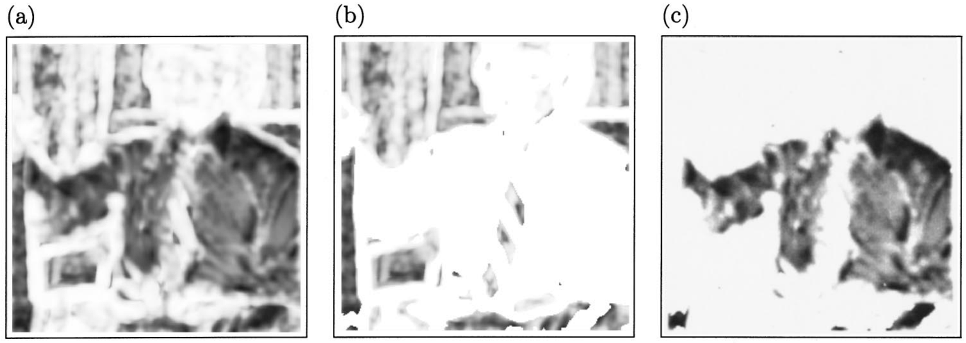

Fig. 14 Estimation of the risk of aliasing: (a) uncleaned version, (b) low energy part, (c) cleaned version.

$$h(\mathbf{v}_{m,n}) = \eta(\mathbf{v}_{m,n}) h_{\mathrm{MS}}(\mathbf{v}_{m,n}) + (1-\eta(\mathbf{v}_{m,n})) h_{\mathrm{EP}}(\mathbf{v}_{m,n}). \tag{26}$$

(The low resolution of the gravure printing screen lattice makes bilinear interpolation a good choice as the edge-preserving filter.) Note that the risk values were calculated on the source lattice $\mathbf{R}$ instead of on the target lattice $\mathbf{V}$, but that in Eq. (26) values on the target lattice are needed; in practice $\eta(\mathbf{v}_{m,n})$ is estimated as $\eta(\mathbf{r}_{m',n'})$ where $\mathbf{r}_{m',n'}$ is nearest the lattice site of $\mathbf{R}$ to $\mathbf{v}_{m,n}$.

The *local* frequency characteristics of the linear adaptive filter can be easily investigated using the linearity of the Fourier transform:

$$\mathcal{F}\{\alpha_1 g_{\mathrm{MS}}(x) + \alpha_2 g_{\mathrm{EP}}(x)\} = \alpha_1 G_{\mathrm{MS}}(f) + \alpha_2 G_{\mathrm{EP}}(f). \tag{27}$$

Figure 10 shows the half amplitude (-6 dB) contour in the two-dimensional frequency plane for various values of the risk η. It is apparent for $\eta=0$ that most frequencies arealmost unattenuated by the bilinear interpolation filter. For higher values of η, the passband narrows because the filter shifts towards the surface projected cubic B spline; as a consequence, a typical low-pass filter is created.

4 Results

Figures 11(a), 12(a), and 13(a) show three test images and several resampled versions (b)–(d) making use of linear resampling techniques. The figures in (a) are the original images, reproduced as well as possible by the printing process used for this paper. The figures (b)–(d) are resampled versions on the screen lattice of gravure printing and are thus reproduced by our simulation for gravure printing halftoning. The first image ''shirt'' (Fig. 11) is a natural ''photographic'' picture (256×256 pixels). The second image ''zoneplate'' (Fig. 12) is a synthetic image (256×256 pixels), and has already been introduced in Sec. 3.1.2. In principle the original images should be free of aliasing. However it is likely that the printing process used to reproduce this paper will introduce some moiré in Fig. 12(a). The third image ''horloge'' (Fig. 13) is again a ''photographic'' example (256×256), showing some fabrics and fine text details.

Obviously nearest neighbor and bilinear resampling [Figs. 11–13 parts (b) and (c)] are not adequate: clearly visible moiré patterns arise in the high frequency regions of all three images. These artifacts are not exceptional for this

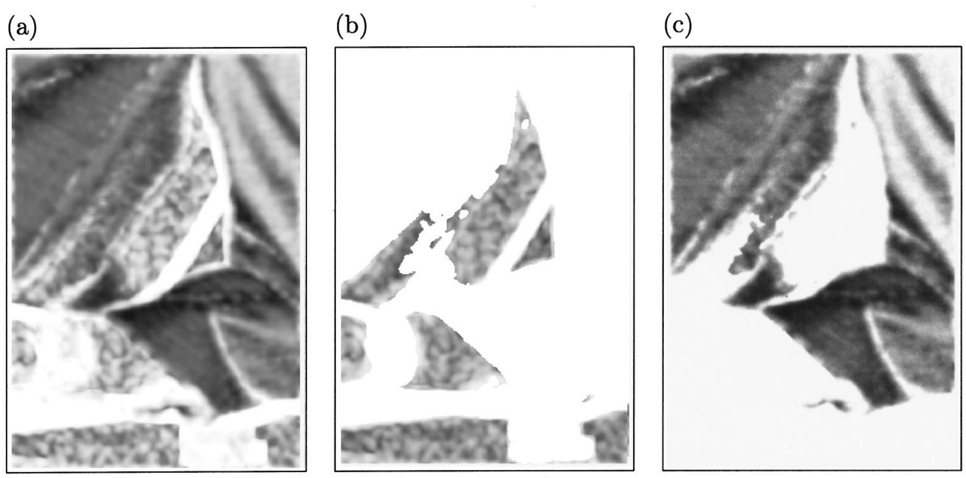

Fig. 15 Estimation of the risk of aliasing: (a) uncleaned version, (b) low energy part, (c) cleaned version.

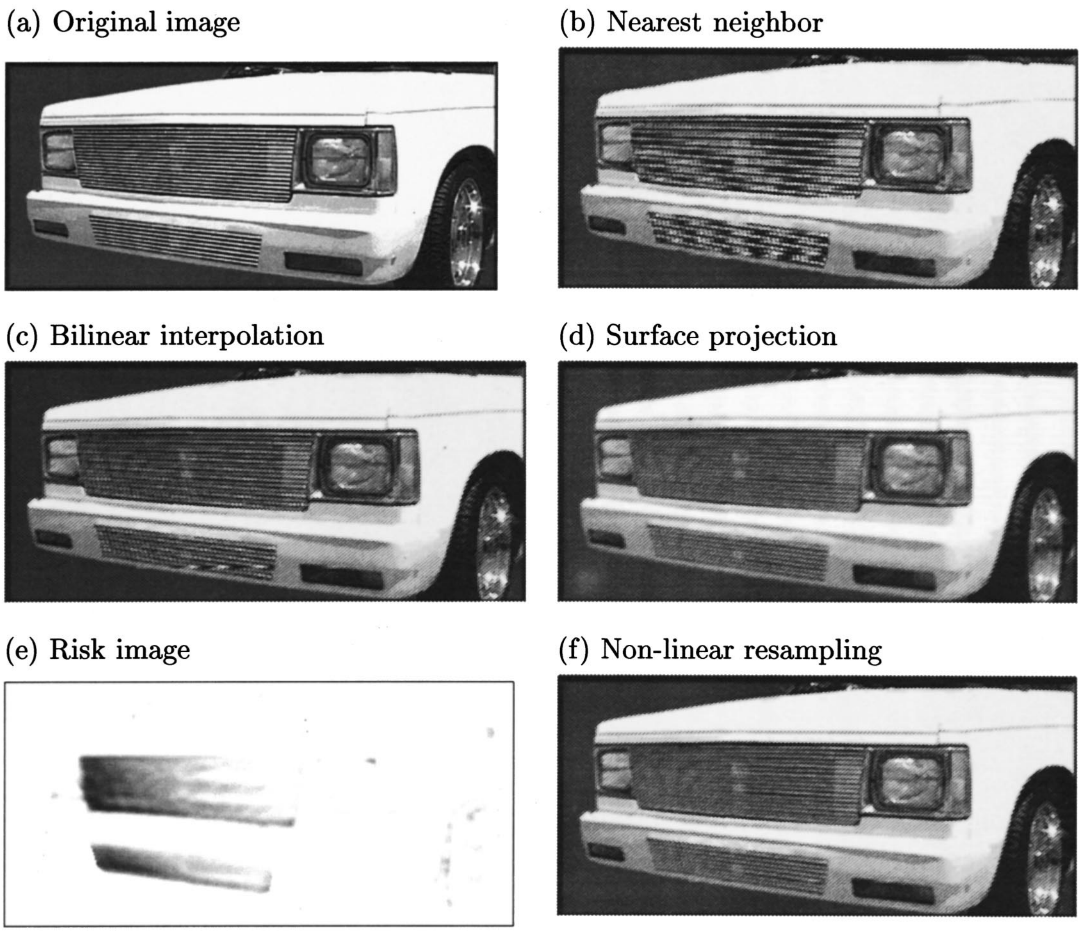

Fig. 16 (a) Additional test image ''car'' with (b)–(d) linear resampled versions, (e) risk image, and (f) result after nonlinear resampling.

kind of gravure printing. Fabrics in clothes, heavy textures such as burlap material, and dot and line patterns from grills could easily give rise to moiré.

The results of Figs. 11(d), 12(d), and 13(d) show that a linear resampling filter can also suppress moiré. The images were resampled using a cubic *B*-spline interpolation function combined with the surface projection principle. Unfortunately, the extra low-pass filtering also significantly blurs the image. Such global smoothing is mostly unacceptable.

Figures 14 and 15 show the risk images for ''natural'' images. The risk images of Figs. 14(a) and 15(a) were obtained by not checking the denominator of the risk against a threshold value. Almost the whole risk image is having a high risk value: most of the ''background'' is risky as well. Figures 14(b) and 15(b) show only that part of the risk image where the denominator of η is below the threshold value. The final corrected risk images are shown in Figs. 14(c) and 15(c).

Figures 11(f), 12(f), and 13(f) show the images resampled by the novel nonlinear approach based on the risk images in Figs. 11(e), 12(e), and 13(e). Comparing these results with the resampled images using bilinear interpolation and cubic *B* spline must show we combined the best of both. For example, the face in ''shirt'' is clearly sharper than when using only surface projection as in Fig. 11(d), although the moiré patterns of Fig. 11(c) are suppressed as well. The ''zoneplate'' also gives a good result thanks to the smoothness of the risk image in the neighborhood of the Nyquist criterion. Finally, the ''horloge'' also gives good results. The fine details such as the wristwatch and the textual information are preserved well, while the moiré patterns of the striped clothes are suppressed. Figure 16 shows an additional test image ''car'' with a grill containing high frequency components. Visual inspection shows the nonlinear resampling scheme combines the sharpness of bilinear interpolation (e.g., in the wheels and the headlights) with the moiré suppressing properties of surfaced projected cubic *B* spline (in the grill). Additionally, an objective quality measure confirms these results by computing a numerical value for the degree of sharpness and aliasing in the halftoned results.[17]

5 Conclusion

Image resampling is needed for a variety of applications in image processing. This paper considered the case of gravure printing where the image is resampled on a screen lattice which can introduce undesirable moiré patterns. Precautions against such sampling moiré have to be made in the prepress phase, which is not practical and sometimes also not feasible. Currently, simple resampling filters like bilinear interpolation are employed but these are unsatisfactory because they do not adapt to the local image content; when linear filters are sufficiently low pass to prevent moiré, they unacceptably blur the image. We presented a novel technique to adaptively resample an image from its source lattice to an arbitrary target lattice. The output of two suitable linear resampling filters, i.e., bilinear interpolation and cubic *B* spline, are locally weighted according to an estimate of the risk of aliasing. This new resampling scheme aims at joint antialiasing and edge preserving capabilities.

The proposed technique makes use of a windowed DFT. Several window functions were compared regarding two criteria which are important for this application: the ''edge response'' and the ''zoneplate response.'' The Hann window showed the best properties of the considered windows. This technique can also be adapted for other resampling problems (e.g., such as those used in desktop printers) or multidimensional aliasing problems.

Acknowledgments

This work was financially supported by the Fund for Scientific Research-Flanders (Belgium), through a mandate of Research Assistant (Dimitri Van De Ville) and through Project No. G.204194.N. The authors would also like to thank Hans De Witte from Barco Graphics and Professor Jan Van Campenhout from Ghent University.

References

1. O. Bryngdahl, ''Moiré: Formation and interpretation,'' *J. Opt. Soc. Am.* **64**, 1287–1294 (1974).
2. A. Glassner, ''Inside moiré patterns,'' *IEEE Comput. Graphics Appl.* **17**, 97–101 (1997).
3. J. F. Blinn, ''Jim Blinn's Corner: What we need around here is more aliasing,'' *IEEE Comput. Graphics Appl.* **9**, 75–79 (1989).
4. J. F. Blinn, ''Jim Blinn's Corner: Return of the Jaggy,'' *IEEE Comput. Graphics Appl.* **9**, 82–88 (1989).
5. I. Amidror, *The Theory of the Moiré Phenomenon*, Computational Imaging and Vision, Vol. 15, Kluwer Academic, Dordrecht (2000).
6. R. A. Ulichney, *Digital Halftoning*, MIT Press, Cambridge, MA (1987).
7. D. Mitchell and A. Netravali, ''Reconstruction filters in computer graphics,'' *ACM Comput. Graphics* **22**, 221–228 (1988).
8. R. Soininen, ''Digital image resizing methods,'' Master's thesis, Tampere University of Technology, 1994.
9. H. Hou and H. Andrews, ''Cubic splines for image interpolation and digital filtering,'' *IEEE Trans. Acoust., Speech, Signal Process.* **26**, 508–517 (1978).
10. R. Keys, ''Cubic convolution interpolation for digital image processing,'' *IEEE Trans. Acoust., Speech, Signal Process.* **29**, 1153–1160 (1981).
11. A. Rosenfeld and A. C. Kak, *Digital Picture Processing*, 2nd ed., Academic, New York (1982).
12. P. G. Roetling, ''Halftone method with edge enhancement and moiré suppression,'' *J. Opt. Soc. Am.* **10**, 985–989 (1976).
13. I. Defée, R. Soininen, and Y. Neuvo, ''Detail-preserving filters with improved lowpass characteristics,'' *Signal Processing VI: Theories and Applications*, pp. 1157–1160, Elsevier Science, New York (1992).
14. D. Petersen and D. Middleton, ''Sampling and reconstruction of wave-number-limited functions in N-dimensional Euclidean spaces,'' *Inf. Control.* **5**, 279–323 (1962).
15. M. Unser, A. Aldroubi, and M. Eden, ''B-spline signal processing,'' *IEEE Trans. Signal Process.* **41**, 821–848 (1993).
16. W. Press *et al.*, *Numerical Recipes in C*, Cambridge University Press, Cambridge (1992).
17. D. Van De Ville, K. Denecker, W. Philips, and I. Lemahieu, ''On the measurement of aliasing and sharpness in halftones,'' in *Euromedia 2000*, F. Broeckx and L. Pauwels, Eds., pp. 311–316, Society for Computer Simulation International, Antwerp, Belgium, (May 2000).

Dimitri Van De Ville received his engineering degree in Computer Sciences from Ghent University in July 1998. The topic of his thesis was the design of a nonlinear antialiasing filter for gravure printing. This work received the Sidmar Thesis Award 1998 and Barco Thesis Award 1999. Currently he is working toward a PhD at the Medical Image and Signal Processing research group (MEDISIP) at the Department of Electronics and Information Systems (ELIS) at the same university. He received a research assistant grant from the Fund for Scientific Research (FWO-Flanders).

Koen Denecker received his degree in physical engineering from Ghent University in 1995. Currently, he is working toward a PhD as a research assistant of the Fund for Scientific Research (FWO-Flanders), at the Department of Electronics and Information Systems (ELIS) of the same university. His main research topics are lossless and near-lossless compression of halftone and colour images.

Wilfried Philips received his diploma degree in electrical engineering in 1989 and his PhD in applied sciences in 1993, both from Ghent University, Belgium. Since November 1997 he has been a lecturer with the Department of Telecommunications and Information Processing (TELIN) at the same university. His main research interests are image data compression, image restoration and image analysis.

Ignace Lemahieu graduated with a degree in physics from Ghent University in 1983, and obtained his doctoral degree in physics in 1988 from the same university. He joined the Department of Electronics and Information Systems (ELIS) in 1989 as a research associate with the Fund for Scientific Research (FWO-Flanders), Belgium. He is now a professor of medical image processing and head of the MEDISIP research group. His research interests comprise all aspects of image processing and biomedical signal processing, including image reconstruction from projections, pattern recognition, image fusion and compression. He is the coauthor of more than 150 papers. He is a member of IEEE, SPIE, ESEM (European Society for Engineering and Medicine) and EANM (European Association of Nuclear Medicine).